

FLUID MECHANICS

REVIEW ON THE INSTABILITY AND OPTICS OF CAPILLARY JETS AND GLASS FIBRES: A FRUITFULL COLLABORATION BETWEEN INSTITUTE OF MECHANICS AND IUSTI*

ST. RADEV

*Institute of Mechanics, Bulgarian Academy of Sciences,
Acad. G. Bonchev St., Bl. 4, 1113 Sofia, Bulgaria,
e-mail: stradev@imbm.bas.bg*

F. R. A. ONOFRI, A. LENOBLE, L. TADRIST

*IUSTI UMR 7343 CNRS/Aix-Marseille University,
5 r. E. Fermi, Technopôle de Château Gombert, Marseille 13453, France,
e-mails: Fabrice.Onofri@polytech.univ-mr.fr, Anne.lenoble@laposte.net,
Lounes.Tadrisk@polytech.univ-mr.fr*

[Received 19 November 2012. Accepted 03 June 2013]

ABSTRACT. The paper review key results [1-14] of the joint researches conducted by IMech and IUSTI. In the First part, we review models and experimental results on the linear and nonlinear instability of a capillary jet including both axisymmetric and nonaxisymmetric disturbances. In the Second part, results on draw resonances, occurring during a glass fibre process are reviewed, as well as the unique optical models and methods developed to perform these studies.

KEY WORDS: capillary jets, instability, glass fibre drawing, optical particle sizing, light scattering.

1. Introduction

The IMech and IUSTI institutes have conducted a long term join research project which deserves to be reviewed herein [1-14]. Three major and

*We would like to express our gratitude to the CNRS (projects PECO/NEI) and BAS for supporting our collaboration. As well we thank for their financial support the Bulgarian Science Fund under the Project DCVP02/1, the French Agency for the Environment and Energy Resources (ADEME) and Saint-Gobain Recherche.

Corresponding author e-mail: stradev@imbm.bas.bg

intricate contributions may be identified: capillary jet instabilities, draw resonances occurring in glass fibre processes, and optical methods and models to characterize experimentally these instabilities. To save space and regarding to the scope of the present journal, optical developments will only be briefly reviewed in combination with draw resonances instabilities. So that, from a general point of view, the present paper is organized in two parts. The first part (i.e. section 2) deals with the instability of capillary jets. Indeed, it is known that the flow of a liquid jet injected through a nozzle in another immiscible liquid is known as unstable due to the capillary forces at the interface that tend to minimize the cylindrical jet surface by transforming it into drops. The instability begins by a propagation of small axisymmetric disturbances of the jet radius with growing amplitudes that finally acquire the value of the undisturbed radius provoking the jet break-up. Although, the latter is mainly controlled by the surface tension, some other factors could play an important role, as well. The factors that are of interest for the present paper are the injection velocity (inertial forces) and the surrounding fluid density (aerodynamic forces) acting on the jet surface. In the second part (i.e. section 3) of this paper, we mostly review the work performed on draw resonances. The starting point of these studies, conducted with Saint-Gobain Recherche, was to provide data and models to understand the discrepancy between industrial knowledge's and the prediction of stability models found in the literature. Indeed, in industry glass drawing processes can be operated with draw ratios up 10^5 , whereas models predict that self sustained oscillations of the tension of the drawn filament may induce fibre breaking when the draw ratio exceeds 10^4 . Section 4 is a brief conclusion pointing out the achievements of this fruitful collaboration as well as on the institutions which have supported this work.

2. Instability of a capillary jets

2.1. Statement of the problem for the flow and instability of a capillary jet-general case

Consider a steady axisymmetric liquid jet of density γ and viscosity μ flowing down into an inviscid immiscible fluid of density γ_1 [10-12]. The steady jet flow (referred further as undisturbed) is assumed of constant radius a_0 and uniform axial velocity W with respect to a cylindrical coordinate system $O\rho\varphi z$, whose Oz axis lies on the jet axis, directed downstream (see Fig. 1). The corresponding velocity of the outer fluid is denoted by W_1 .

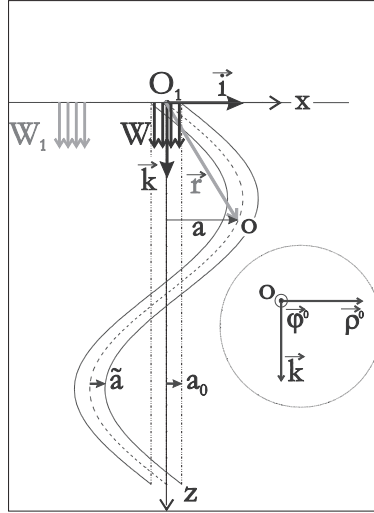


Fig. 1. Undisturbed and disturbed flow condition.

2.1.1. Equations of motion

In cylindrical coordinates the equations of motion for a non-axisymmetrical jet could be written in the following form:

$$(1) \quad \frac{\partial \vec{v}}{\partial t} + \vec{v} \cdot \nabla \vec{v} + \vec{X} = -\frac{1}{\gamma} \nabla p + \frac{1}{\gamma} (\nabla \Pi + \vec{Y}),$$

where t denotes the time, $\vec{v}(v, w, u)$ – the radial, transversal and axial component of the velocity, respectively, p – the pressure and $\Pi(\vec{p}_\rho, \vec{p}_\phi, \vec{p}_z)$ – the well known tensor of the viscous stresses, $\nabla = \vec{\rho}^\circ \frac{\partial}{\partial \rho} + \vec{\varphi}^\circ \rho^{-1} \frac{\partial}{\partial \varphi} + \vec{k} \frac{\partial}{\partial z}$ – the gradient operator with $\vec{\rho}^\circ$, $\vec{\varphi}^\circ$, \vec{k} as coordinate vectors. The additional symbols \vec{X} and \vec{Y} are defined as:

$$(2) \quad X_\rho \equiv -\rho^{-1} w^2, X_\phi \equiv -\rho^{-1} v w, X_z \equiv 0,$$

$$(3) \quad Y_\rho \equiv \rho^{-1} (p_{\rho\rho} - p_{\phi\phi}), Y_\phi \equiv 2\rho^{-1} p_{\rho\phi}, Y_z \equiv \rho^{-1} p_{\rho z}.$$

External forces are neglected. The corresponding continuity equation has the form:

$$(4) \quad \nabla \cdot \vec{v} + \rho^{-1} v = 0.$$

2.1.2. Interface geometry

The interface (jet surface) equation is written into a form allowing non-axisymmetrical disturbances:

$$(5) \quad \vec{r} = \vec{R}_s = a(\varphi, z, t) \vec{\rho}^\circ,$$

where a denotes the cross-section radius. Let \vec{t}_φ and $\vec{t}_z \equiv \vec{\psi}$ be the tangential vectors to the interface along the corresponding coordinate lines, namely:

$$(6) \quad \vec{t}_\varphi = \frac{\partial \vec{R}_s}{\partial \varphi} = G^{-1} \left(\frac{\partial a}{\partial \varphi} \vec{\rho}^\circ + a \vec{\varphi}^\circ \right), \quad G = \left| \frac{\partial \vec{R}_s}{\partial \varphi} \right|,$$

$$(7) \quad \vec{\psi} = \frac{\partial \vec{R}_s}{\partial z} = E^{-1} \left[\frac{\partial a}{\partial z} \vec{\rho}^\circ + \vec{k} \right], \quad E = \left| \frac{\partial \vec{R}_s}{\partial z} \right|.$$

Then the outside interface normal vector reads:

$$(8) \quad \vec{N} = N^{-1} \vec{t}_\varphi \times \vec{\psi} = N^{-1} \left(a \vec{\rho}^\circ - \frac{\partial a}{\partial \varphi} \vec{\varphi}^\circ - a \frac{\partial a}{\partial s} \vec{k} \right), \quad N = \left| \vec{t}_\varphi \times \vec{\psi} \right|.$$

Further on for convenience a new tangential vector $\vec{\phi}$ will be used:

$$(9) \quad \vec{\phi} = \vec{\psi} \times \vec{N},$$

assuring that the trihedron $(\vec{\phi}, \vec{\psi}, \vec{N})$ is orthonormal.

2.1.3. Interface boundary conditions

When written in a scalar form the force balance at the interface is reduced to three boundary conditions for the normal and two tangential stresses:

$$(10) \quad \begin{aligned} & \left[\left[-p + (\Pi \cdot \vec{N}) \cdot \vec{N} \right] \right]_N = -\frac{\sigma}{R_m}, \\ & \left[\left[(\Pi \cdot \vec{N}) \cdot \vec{\phi} \right] \right]_N = 0, \\ & \left[\left[(\Pi \cdot \vec{N}) \cdot \vec{\psi} \right] \right]_N = 0, \end{aligned}$$

where σ denotes the surface tension coefficient, while R_m – the mean curvature radius of the interface, whose equation is given as follows:

$$(11) \quad R_m^{-1} = \frac{E^2 L_s - 2F_s M_s + G^2 N_s}{(EG)^2 - F_s^2},$$

where

$$(12) \quad \begin{aligned} F_s &= \vec{t}_\varphi \cdot \vec{t}_z = \frac{\partial a}{\partial \varphi} \frac{\partial a}{\partial z}, \quad L_s = \vec{N} \cdot \frac{\partial^2 \vec{R}_s}{\partial \varphi^2} = N^{-1} \left[a \left(\frac{\partial^2 a}{\partial \varphi^2} - a \right) - 2 \left(\frac{\partial a}{\partial \varphi} \right)^2 \right], \\ M_s &= \vec{N} \cdot \frac{\partial^2 \vec{R}_s}{\partial \varphi \partial z} = N^{-1} \left(a \frac{\partial^2 a}{\partial \varphi \partial z} - \frac{\partial a}{\partial \varphi} \frac{\partial a}{\partial z} \right), \quad N_s = \vec{N} \cdot \frac{\partial^2 \vec{R}_s}{\partial z^2} = N^{-1} a \frac{\partial^2 a}{\partial z^2}. \end{aligned}$$

Note that in the eqs (10) the symbol $[[A]]_N$ denotes the (potential) discontinuity of an arbitrary parameter A at the interface in the direction of the outside normal:

$$(13) \quad [A]_N = A_2^* - A_1^*, \quad A^* \equiv A(\rho = a).$$

Due to the immiscibility between the jet and surrounding fluid the zero-mass flux condition should be satisfied at both sides of the interface:

$$(14) \quad a \frac{\partial a}{\partial t} = av^* - \frac{\partial a}{\partial \varphi} w^* - a \frac{\partial a}{\partial z} u^*.$$

2.2. Linearized equations of motion and boundary conditions for the disturbances

As mentioned above, our stability analysis [12] concerns a steady jet of a radius a_0 and axial velocity W independent on both the radial and the axial coordinates. Further on, we will study the evolution of small disturbances (denoted by superscript tilde), imposed on the steady flow:

$$(15) \quad v = \tilde{v}, \quad w = \tilde{w}, \quad u = W + \tilde{u}, \quad p = P + \tilde{p}, \quad a = a_0 + \tilde{a},$$

where P denotes the constant undisturbed pressure. Substituting the above expressions into eqs. (1)-(4) and neglecting the products of the disturbed terms results into linearized equations of motion of the following form:

$$(16) \quad \begin{aligned} B(\tilde{v}) &= -\frac{1}{\gamma} \frac{\partial \tilde{p}}{\partial \rho} + \frac{\mu}{\gamma} \left(\Delta \tilde{v} - 2\rho^{-2} \frac{\partial \tilde{w}}{\partial \varphi} \right) \\ B(\tilde{w}) &= -\frac{1}{\gamma} \rho^{-1} \frac{\partial \tilde{p}}{\partial \varphi} + \frac{\mu}{\gamma} \left(\Delta \tilde{w} + 2\rho^{-2} \frac{\partial \tilde{v}}{\partial \varphi} \right), \\ B(\tilde{u}) &= -\frac{1}{\gamma} \frac{\partial \tilde{p}}{\partial z} + \frac{\mu}{\gamma} \Delta \tilde{u} \end{aligned}$$

and

$$(17) \quad \rho^{-1} \frac{\partial}{\partial \rho} (\rho \tilde{v}) + \rho^{-1} \frac{\partial \tilde{w}}{\partial \varphi} + \frac{\partial \tilde{u}}{\partial z} = 0,$$

where μ denotes the viscosity, Δ is Laplace operator in cylindrical coordinates, B is newly defined linear operator as:

$$(18) \quad B \equiv \frac{\partial}{\partial t} + W \frac{\partial}{\partial z}.$$

Similarly the boundary conditions (10) and (14) appear in the following linearized form:

$$(19) \quad \tilde{p}^* - \tilde{p}_1^* - 2\mu \left(\frac{\partial \tilde{v}}{\partial \rho} \right)^* = -\frac{\sigma}{a_0} \left(\frac{\tilde{a}}{a_0} + \frac{1}{a_0} \frac{\partial^2 \tilde{a}}{\partial \varphi^2} + a_0 \frac{\partial^2 \tilde{a}}{\partial z^2} \right),$$

$$(20) \quad \begin{aligned} \left(\frac{\partial \tilde{w}}{\partial \rho} \right)^* + a_0^{-1} \left[\left(\frac{\partial \tilde{v}}{\partial \varphi} \right)^* - \tilde{w}^* \right] &= 0; \\ \left(\frac{\partial \tilde{u}}{\partial \rho} \right)^* + \left(\frac{\partial \tilde{v}}{\partial z} \right)^* &= 0 \end{aligned} ,$$

and

$$(21) \quad B(\tilde{a}) = \tilde{v}^*,$$

where A^* here and below on is used for the value $A(\rho = a_0)$.

2.3. Equations for the amplitudes of the disturbances

In the context of the linear theory of instability [12], we will search a solution of the eqs. (16)–(17) and the corresponding boundary conditions (19)–(21) in the form of separate modes:

$$(22) \quad \tilde{v} = \bar{v} e^{i\xi}, \quad \tilde{w} = \bar{w} e^{i\xi}, \quad \tilde{u} = \bar{u} e^{i\xi}, \quad \tilde{p} = \bar{p} e^{i\xi}, \quad \tilde{a} = \bar{a} e^{i\xi},$$

where the corresponding amplitudes (except $\bar{a} = \text{const}$) are assumed unknown functions of the radial coordinate ρ . The new independent variable ξ is defined as:

$$(23) \quad \xi = \omega t - kz + n\varphi,$$

where k is a given wave number, n – a number of the asymmetric mode, when $n > 0$, while $\omega = \omega_r + i\omega_i$ denotes the unknown complex angular frequency of the disturbances. Substituting eqs. (22) into equations of motion of the jet (16) and continuity equation (17) result in the following system of ordinary differential equations:

$$\begin{aligned}
 ic_*\bar{v} &= -\frac{1}{\gamma}\bar{p}' + \frac{\mu}{\gamma} [L_n\bar{v} - \rho^{-2}(\bar{v} + 2in\bar{w})], \\
 ic_*\bar{w} &= -\frac{in}{\gamma}\rho^{-1}\bar{p} + \frac{\mu}{\gamma} [L_n\bar{w} + \rho^{-2}(2in\bar{v} - \bar{w})], \\
 ic_*\bar{u} &= \frac{ik}{\gamma}\bar{p} + \frac{\mu}{\gamma}L_n\bar{u}
 \end{aligned}
 \tag{24}$$

and

$$\bar{v} + \rho^{-1}(\bar{v} + in\bar{w}) - ik\bar{u} = 0,
 \tag{25}$$

where the superscript prime denotes a differentiation in respect to ρ and the ordinary differential operator L_n is defined as:

$$L_n \equiv \frac{d^2}{d\rho^2} + \rho^{-1}\frac{d}{d\rho} - (k^2 + n^2\rho^{-2}).
 \tag{26}$$

Additionally, for convenience the following new unknown parameter is introduced:

$$c_* \equiv \omega - kW.
 \tag{27}$$

When the disturbances in the surrounding fluid are concerned the continuity equation remains unchanged, while the equations of motion are easily obtained from eqs. (24), taking into account that the fluid is a nonviscous one ($\mu_1 = 0$):

$$\begin{aligned}
 ic_{1*}\bar{v}_1 &= -\frac{1}{\gamma_1}\bar{p}'_1, \\
 ic_{1*}\bar{w}_1 &= -\frac{in}{\gamma_1}\rho^{-1}\bar{p}_1, \\
 ic_{1*}\bar{u}_1 &= \frac{ik}{\gamma_1}\bar{p}_1
 \end{aligned}
 \tag{28}$$

where now

$$c_{1*} = \omega - kW_1.
 \tag{29}$$

In fact the above equations relate the velocity amplitudes \bar{v}_1 , \bar{w}_1 and \bar{u}_1 to the pressure amplitude \bar{p}_1 in the surrounding fluid. When the continuity equation is used to eliminate these amplitudes, we simply obtain an equation for the surrounding pressure:

$$(30) \quad L_n \bar{p}_1 = 0,$$

which corresponds to an irrotational flow in the surrounding fluid. In the next section, we will use the fact that eq. (30) is easily transformed to a modified Bessel equation.

2.4. Analytical solution for the amplitudes. Dispersion equation

As mentioned above, the solution of eq. (30) could be written as:

$$(31) \quad \bar{p}_1 = A_1 K_n(k\rho),$$

where A_1 is an integration constant, $K_n(\zeta)$ is a modified Bessel function of a n -th order and of a second kind. In eq. (31), the corresponding Bessel function of a first kind is eliminated, for it is unbounded at $\rho = \infty$.

The solution of eqs. (24)–(25) can be splitted into an irrotational (non-viscous) and viscous part, respectively:

$$(32) \quad \bar{v} = \bar{v}_{ir} + \bar{v}_v, \quad \bar{w} = \bar{w}_{ir} + \bar{w}_v, \quad \bar{u} = \bar{u}_{ir} + \bar{u}_v.$$

Similar to the surrounding flow, the irrotational part of the jet flow satisfies pressure equation (30) in which the subscript “1” should be omitted. Therefore, the irrotational velocity modes can again be expressed by the jet pressure:

$$(33) \quad \bar{p} = A I_n(k\rho).$$

The equations for the viscous velocity amplitudes are similar to eqs. (24) providing that the pressure terms are neglected:

$$(34) \quad \begin{aligned} i c_* \bar{v}_v &= \frac{\mu}{\gamma} [L_n \bar{v}_v - \rho^{-2} (\bar{v}_v + 2inw_v)], \\ i c_* \bar{w}_v &= \frac{\mu}{\gamma} [L_n \bar{w}_v + \rho^{-2} (2in\bar{v}_v - \bar{w}_v)], \\ i c_* \bar{u}_v &= \frac{\mu}{\gamma} L_n \bar{u}_v \end{aligned}$$

It should be mentioned that the above system is selfconsistent: assuming that the velocity amplitudes in the left side of eqs. (34) satisfy the continuity equation (25) the same is true for the corresponding right sides. As seen, the last of equations (34) is separated from the remaining equations and can be solved independently. By introducing a modified wave number k_1 :

$$(35) \quad k_1^2 = k^2 + i \frac{\gamma C_*}{\mu},$$

the equation for \bar{u}_v is transformed to a form similar to eq. (30), if the wave number k is replaced by k_1 :

$$(36) \quad L_{n,1} \bar{u}_v = 0, \quad L_{n,1} \equiv \frac{d^2}{d\rho^2} + \rho^{-1} \frac{d}{d\rho} - (k_1^2 + n\rho^{-2}).$$

Therefore:

$$(37) \quad \bar{u}_v = BI_n(k_1\rho).$$

Dispersion equation. By introducing new unknowns:

$$(38) \quad v_{\pm} = \bar{v}_v \pm \bar{w}_v,$$

the first two of eqs. (34) can be splitted into two independent modified Bessel equations of type (36) with left hand sides $L_{n+1,1}v_+$ and $L_{n-1,1}v_-$, respectively. As a result we obtain:

$$(39) \quad \bar{v}_v = CI_2(k_1\rho) + DI_0(k_1\rho), \quad \bar{w}_v = CI_2(k_1\rho) - DI_0(k_1\rho).$$

Substituting into the continuity equation, the following relationship is derived for the constants of integration:

$$(40) \quad B = -i \frac{k_1}{k} (C + D).$$

By using eq. (39) and the interface boundary conditions (19)–(21), the remaining integration constants A, A_1, C, D , can be determined as functions of the (arbitrary) amplitude \bar{a} . After rather tedious, but straightforward calculations the dispersion equation can be written in the form of a determinant of a fourth order:

$$(41) \quad \Delta_{44} = |a_{mn}| = 0, \quad (m, n = 1, \dots, 4),$$

where

$$(42) \quad \begin{array}{ll} a_{11} = iq\dot{I}_n & a_{12} = \hat{I}_{n+1} \\ a_{13} = \hat{I}_{n-1} & a_{14} = ic_*^\circ \\ a_{21} = 2iq^3\dot{I}_n & a_{22} = q_1^2\hat{I}_n + q^2\hat{I}_{n+1} \\ a_{23} = q_1^2\hat{I}_n + q^2\hat{I}_{n-1} & a_{24} = 0 \\ a_{31} = 2in(I_n - q\dot{I}_n) & a_{32} = q_1\hat{I}_{n+1} - (n+1)\hat{I}_{n+1} \\ a_{33} = -q_1\hat{I}_{n-1} - (n-1)\hat{I}_{n-1} & a_{34} = 0 \\ a_{41} = c_*^\circ I_n - 2iRe^{-1}q^2\ddot{I}_n & a_{42} = -2Re^{-1}q_1\hat{I}_{n+1} \\ a_{43} = -2Re^{-1}q_1\hat{I}_{n+1} & a_{44} = -A_{44} \end{array}$$

with:

$$(43) \quad c_*^\circ = \frac{a_\circ}{W} c_* = \omega^\circ, \quad c_{1*}^\circ = \frac{a_\circ}{W} c_{1*} = \omega^\circ + W_1^\circ q,$$

$$(44) \quad -A_{44} = \gamma_1^\circ c_{1*}^{\circ 2} \frac{K_n}{q \dot{K}_n} + W e^{-1} (q^2 + n^2 - 1).$$

Note that eqs. (41) and (42) are transformed into a non-dimensional form, hence they contain the non-dimensional parameters of the problem: Reynolds number $Re = \gamma a_0 W / \mu$, Weber number $We = \gamma a_0 W^2 / \sigma$ and non-dimensional density and undisturbed velocity ratio $\gamma_1^\circ = \gamma_1 / \gamma$, $W_1^\circ = W_1 / W$, respectively. Similarly $\omega^\circ = a_0 \omega / W$ is the nondimensional complex angular frequency, $q = a_0 k$ and $q_1 = a_0 k_1$ - the nondimensional wave and modified wave number, respectively.

It should be mentioned, that when the argument of Bessel functions is equal to $\zeta = k\rho$, it is omitted, while it is denoted by superscript \wedge when equals $\zeta_1 = k_1\rho$. Differentiation with respect to the corresponding argument of Bessel function is denoted by supper script dot. In addition, in all Bessel functions $\rho = a_0$. When writing eqs. (42) it is assumed that the reference coordinate system $O\rho\phi z$ is moving with the undisturbed jet flow, while the surrounding fluid is flowing uniformly with a velocity $-W_1^\circ$ parallel to the undisturbed jet axis Oz .

After some obvious algebraic operations on the rows of the determinant Δ_{44} the latter can be reduced to a linear combination of second order determinants. Finally, the dispersion equation appears in the following nondimensional form:

$$(45) \quad c_*^{\circ 2} \frac{I_1}{q \dot{I}_1} \left(1 + \frac{\Delta_1}{\Delta} \hat{I}_2 + \frac{\Delta_2}{\Delta} \hat{I}_0 \right) - 2i Re^{-1} c_*^\circ \frac{q \ddot{I}_1}{I_1} \left(1 + \frac{\Delta_1}{\Delta} \hat{I}_2 + \frac{\Delta_2}{\Delta} \hat{I}_0 \right) + \\ + 2i Re^{-1} c_*^\circ q_1 \left(\frac{\Delta_1}{\Delta} \hat{I}_2 + \frac{\Delta_2}{\Delta} \hat{I}_1 \right) = W e^{-1} q^2 + c_{1*}^{\circ 2} \gamma_1^\circ \frac{K_1}{q \dot{K}_1}.$$

The second order determinants read:

$$(46) \quad \Delta \equiv \begin{vmatrix} a_{22} - 2\hat{q}^2 \hat{I}_2 & a_{23} - 2\hat{q}^2 \hat{I}_0 \\ a_{32} - 2b \hat{I}_2 & a_{33} - 2b \hat{I}_0 \end{vmatrix}, \\ \Delta_1 \equiv 2 \begin{vmatrix} \hat{q}^2 & a_{23} - 2\hat{q}^2 \hat{I}_0 \\ b & a_{33} - 2b \hat{I}_0 \end{vmatrix}, \quad \Delta_2 \equiv 2 \begin{vmatrix} a_{22} - 2\hat{q}^2 \hat{I}_2 & \hat{q}^2 \\ a_{32} - 2b \hat{I}_2 & b \end{vmatrix}.$$

Where:

$$b \equiv \frac{I_1}{\hat{q}I_1'} - 1.$$

The unknown in eq. (45) is the complex frequency $\omega^\circ = \omega_r^\circ + i\omega_i^\circ$, where the imaginary part ω_i° stands for the growth rate of the disturbances and ω_r°/q for the speed of the propagation of the disturbances. In our notations (see eqs. (22)–(23)), the sinuous instability takes place when the growth rate is negative: $\omega_i^\circ < 0$. In the general case, the dispersion equation can be solved only numerically.

2.5. Nonlinear instability of an axisymmetric capillary jet

The linear instability of isolated or submerged in another liquid jet is studied extensively, since Rayleigh [15] by many authors (see, e.g. [16]). In Chacha et al. [2] a direct simulation of the process of disintegration of a viscous liquid column in another immiscible liquid bounded by a tube. A complete numerical solution of the full Navier-Stokes equations (1) is proposed, which gives both qualitative and quantitative results. The applicability of the numerical procedure is verified in comparison with the results of the linear stability analysis and those of Shokoohi [17] and, Shokoohi and Elrod [18], in the case of a liquid column in an inviscid nearly-zero-density fluid. For a column in a viscous liquid phase, the verification is performed on the basis of the results of Tomotika [19] and, Mikami and Mason [20]. The numerical results for the main and satellite drop sizes are compared as well to the corresponding experimental values as measured by Kitamura et al. [21], when the relative velocity of both phases is maintained equal to zero.

As shown in Fig. 2a, initial cosinusoidal disturbance retains its form at the first stages of its evolution in time. Due to the appearance of multiple harmonics, the surface profile is transformed to a noncosinusoidal form, which contains a satellite drop attached to the main one.

The size of the satellite is strongly connected (see Fig. 2b) to the wavelength (wave number). The amplification rate of the temporally growing disturbances is time dependent except for the initial time interval. Additional results could be found in [2].

2.6. Asymmetric (sinuous) jets

2.6.1. Dispersion equation for a sinuous instability of a non-viscous jet

Sinuous instability corresponds to $n = 1$. In a general case for studying the sinuous instability of a viscous jet, the dispersion equation (44) should be solved numerically. However, it is interesting to compare our equation with that

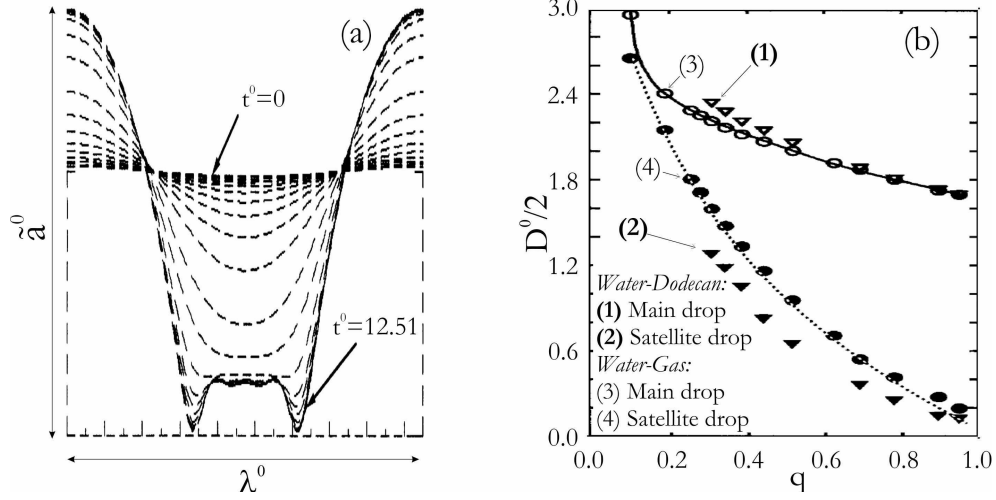


Fig. 2 (a) Evolution of the interface in time. (Water~dodecan: $a_0 = 0.00175$ cm, $\tilde{a}^0/a_0 = 0.02$, $q = 0.66$, $\sqrt{We}/Re = 0.031$; Three stages are observed: cosinusoidal evolution, appearance of a ‘plateau’, formation of a satellite and breakup. (b) Nondimensional drops radii $D^0/2$ vs nondimensional wavenumber q : water~dodecan system (present [2]) and water-gas system [17]. The nondimensional parameters in Fig. 2 are as follows: $t = t/\sqrt{\rho_1 a_0^3/\sigma}$, $\lambda_0 = \lambda/a_0$ and $D^0 = D/1a_0$, where λ stands for wavelength, ρ_1 for jet’s density and D for main and satellite drops

one for a non-viscous jet ($Re = \infty$). For such a jet, the dispersion equation is reduced to the form obtained by Debye and Daen [22] and by Martinon [23]:

$$(47) \quad \begin{aligned} \omega_r^\circ &= \frac{\gamma_1^\circ q b_{11}}{1 - \gamma_1^\circ b_{11}} \\ \omega_i^{\circ 2} &= -\frac{q^2}{1 - \gamma_1^\circ b_{11}} \left(\frac{\gamma_1^\circ b_{11}}{1 - \gamma_1^\circ b_{11}} + We^{-1} \frac{q \dot{I}_1}{I_1} \right), \end{aligned}$$

where for shortness:

$$(48) \quad b_{11} = \frac{\dot{I}_1 K_1}{I_1 K_1}.$$

In Fig. 3a, the growth rate of the sinuous instability predicted by the Non-Viscous Model (see second of eqs (47) is shown for different values of the Weber number, while the density ratio $\gamma_1^\circ \approx 1.21 \times 10^{-3}$ corresponding to a system water-air, is kept fixed. (Note that $Re = \infty$). As illustrated by Fig. 3a, at fixed density ratio the sinuous instability in a non-viscous jet is controlled by

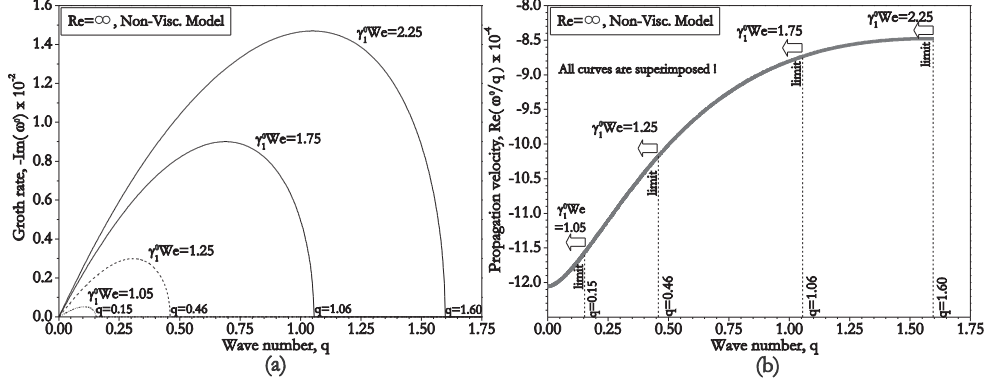


Fig. 3. Non-viscous model for the sinuous instability of a water jet in air: $\gamma_1^0 \approx 1.21 \times 10^{-3}$, injection velocities ranging from $W = 15 : 55$ to $21 : 3$ m/s ($We = 870$ to 1864); (a) growth rate; (b) speed of propagation of the disturbances

the nondimensional combination. More precisely, by using eqs. (47) it could be shown, that the value of $\gamma_1^0 We$ at which the sinuous instability appears, is given by the inequality $\gamma_1^0 We / (1 + \gamma_1^0) \geq 1$. In Fig. 3b, the corresponding curves of the speed of propagation of disturbances are shown. Note that, all curves are superimposed but with a different upper wave number limit, corresponding to the upper end of the instability interval. (For example, for $\gamma_1^0 We = 1.75$ the instability interval ends at $q \leq 1.06$).

2.6.2. Numerical results for the viscous dispersion equation

All calculations performed here are for a water jet in air [24], with radius $a_0 = 300 \mu\text{m}$. Physical properties used for these fluids at ambient temperature are summarized in Table 1.

Table 1. Properties of water and air at $T = 20^\circ\text{C}$

Fluid	ρ [kg/m ³]	σ [mN/m]	μ [10^{-3} kg/m.s]
Water	998.3	73.0	1.00
Air	1.205	–	–

The results in Fig. 4 are obtained by direct solving of the full eq.(44), where curves 4 are shown for comparison and correspond to a non-viscous (model) jet $Re = \infty$. In this figure the effect of Reynolds number on the growth rate and the speed of propagation of the sinuous disturbances are shown starting from a real water jet in air (curve 1).

As expected increasing the jet viscosity in Fig. 4a strongly decreases the maximum growth rate of the disturbances. As shown in Fig. 4b the viscosity

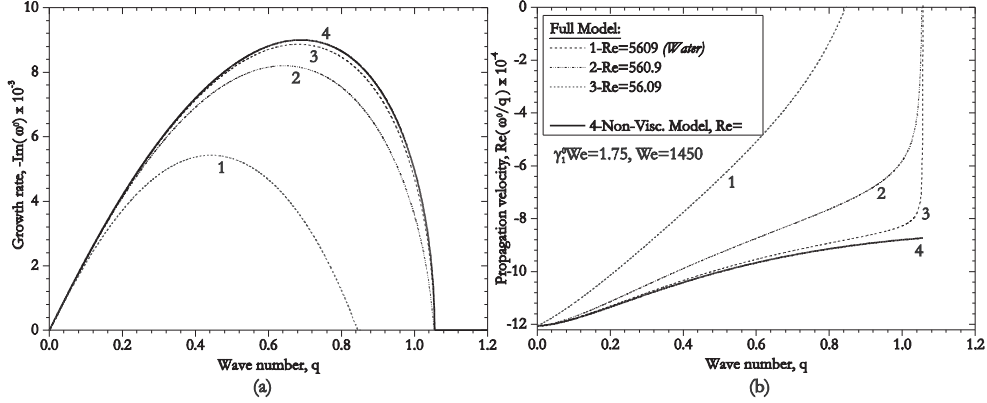


Fig. 4. Effect of the Reynolds number on the growth rate and the speed of propagation of the sinuous disturbances. The basic curve 1 corresponds to a water jet with an injection velocity $W = 18.79$ m/s; the remaining curves correspond to an independent variation of the Reynolds number: (a) growth rate; (b) speed of propagation of disturbances.

tends to decrease the delay of the propagating speed of the disturbances with respect to the jet velocity.

2.6.3. Experiments on jet instability

In Tadrst et al. [25], some experimental results are shown for the instability of a liquid jet leaving a cylindrical nozzle and flowing down another immiscible liquid. A special optical system was used to study the spatial and the temporal interface variations between two liquids. A photoelectric cell was used to measure the light intensity and to obtain the physical parameters of the jet. Spatial analysis revealed a continual contraction of the jet from the nozzle exit to the break-up zone (see Fig. 5a). Fluctuations of the interface over time are characteristic of a random signal with a narrow bandpass. The Fourier transform of the different samples shows a bandpass of finite width centred on a characteristic frequency. The distribution of interface amplitude fluctuations was symmetrical to the average diameter, except in the zone in which the jet breaks up. By systematically tracing the main parameters of the jet diameter, we observed three zones with different jet behaviour.

The characteristic frequency of interface fluctuations increases as a linear function of the distance from the nozzle (Fig. 5b). The amplitude of interface fluctuations was an exponential function of the distance at which jet diameter fluctuations were measured (Fig. 5c).

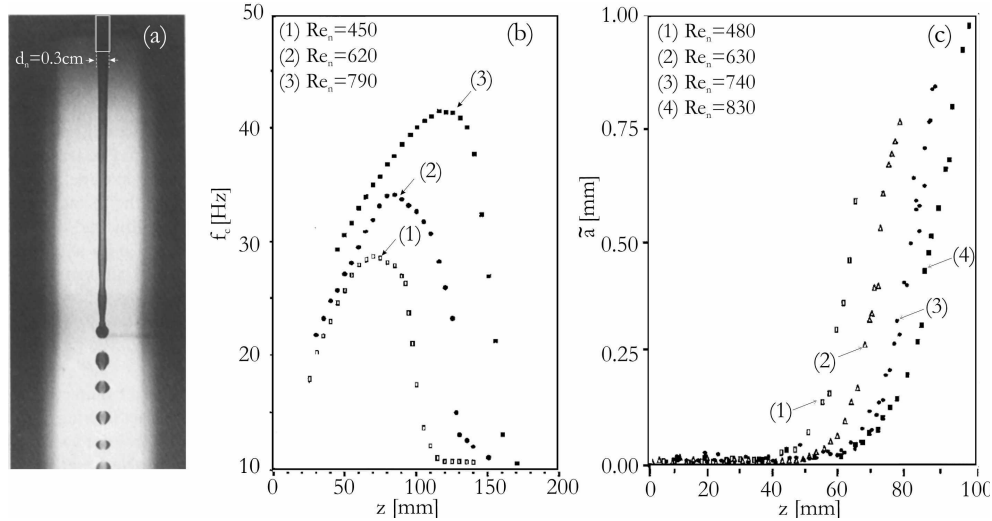


Fig. 5 (a) Jet behaviour at the nozzle exit to the break-up zone in the laminar axisymmetrical regime: $Re = 240$, $a_0 = 0.15$ cm; (b) Characteristic frequency of jet fluctuations f_c versus axial coordinate z for $a_0 = 0.2$ cm and $Re = 225$, 310 and 395; (c) Amplitude of the jet fluctuations variations versus axial coordinate z for $a_0 = 0.15$ cm: $Re = 240$, 315, 370 and 415

3. Instability of a non-isothermal glass drawing process

For more than three decades, it is well established that for a nearly isothermal drawing process draw resonance takes place when the draw ratio (i.e. the ratio of the average fibre velocity at the winder to that at the nozzle, $E = V_f/V_0$) exceeds a value close to $E = 20.21$. For $E = 20.21$, depending on the conditions on the cross section of the nozzle, the fibre diameter may vary non-periodically (quasi-periodically or chaotically, see Yarin et al. [26]; Tyushkevich et al [27]).

Non-isothermal drawing processes, are more particularly those used to produce reinforcement glass fibres, are known to be subject to various perturbations and instabilities which may be harmful from the viewpoints of both manufacturing efficiency (fibre breaking) and quality (diameter fluctuations). Among the possible sources of perturbations are variations in the input parameters (such as glass composition and temperature), variations in winding velocity (drift, vibrations) or certain external factors (Radiative transfer coupling with other nozzles, turbulence generated by the winding). According to some authors (Gliksman [28]; Donnelly and Weinberger [29]; Fisher and Denn [30]; Geyling and Homsy [31]; Schultz and Davis [32]; Gupta et al. [33]; Yarin

et al. [26]), for high viscosity materials such as glasses the most important instability mode is what is referred to as the ‘draw resonance’. This instability is characterized by self sustained oscillations of the tension of the drawn filament (in relation to the diameter) that may induce fibre breaking. Shah and Pearson [34] have been established that the cooling along the spinline strongly stabilizes the process. Gupta et al. [33] found a theoretical maximum of 10^4 as the critical draw ratio although a draw ratio of 10^5 is commonly reached in the industry.

To clarify this point, the present authors have developed a hydrodynamic and thermal model of the drawing process, as well as experimental investigations based on the development of innovative light scattering models and particle sizing instruments. These studies were mostly conducted on glass fibres used in reinforced plastics, in collaboration with the research centre of Saint-Gobain. These fibres are produced by drawing glass melt as it comes out of a bushing nozzle, see Fig. 6a. The fibre solidifies in the draw zone and the solidified jet is wound on a rotating wheel (drum or take-up roller) which provides the required mechanical tension for the fibre in the draw zone. Depending on the composition of the glass, which is determined by various requirements and constraints (end use, melting characteristics, fibre sizing, environmental and cost requirements, etc.) the mean diameters of commonly produced glass filaments are in the range of $D_f = 4 - 25 \mu\text{m}$ (Gupta [35]). In what follows, we first introduce the key parameters and equations of the hydrodynamic and thermal model, then the main characteristic of the light scattering models and finally, the main experimental results are presented.

3.1. Physical model of the non-isothermal drawing process

The problem studied is depicted in Fig. 6a. This geometry, which supposes an axisymmetric process (i.e. $v = 0$, $\partial/\partial\theta = 0$), is used to write the conservation momentum, mass and energy equations of the glass melt jet [28, 35–38, 6]. A Newtonian fluid is assumed, and the boundary conditions and related assumptions are that, (i) there is no mass flux through the surface of the jet; (ii) the glass is incompressible, i.e. $\rho = \text{cte}$, $\vec{\nabla} \cdot \vec{v} = 0$; (iii) the fibre diameter is small $R_0/L \ll 1$, $R(z)/L \ll 1$ and $u/w \ll 1$, so that the radial dependence of the variables u , p and T can be neglected; (iv) the dependence of the viscosity with temperature follows an Arrhenius law; (v) the internal radiation flux, which according to Glicksman [28] is very small, compared to the outer surface radiation flux above 1100°C , as well as the longitudinal conduction are both neglected; (vi) at $z = L$ the take-up velocity is imposed upon solidification; (vii) at $r(t, z)$, friction of air is considered as negligible at atmospheric

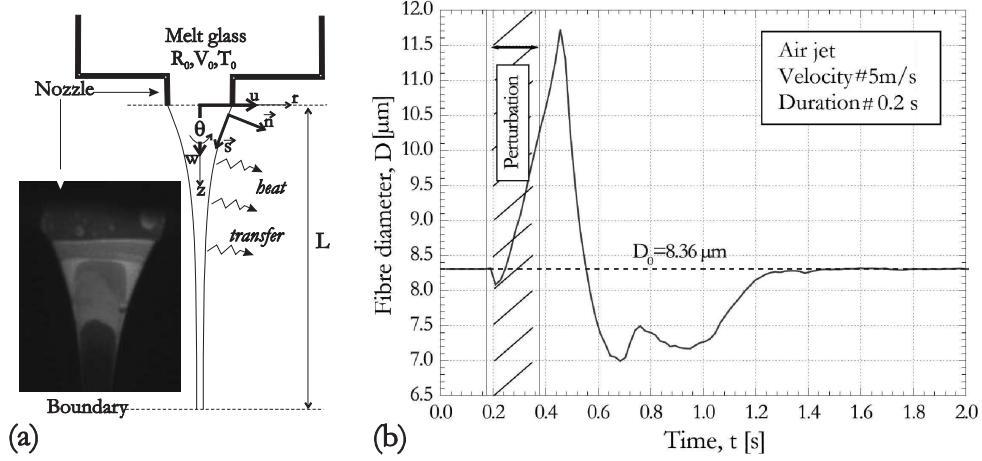


Fig. 6 (a) Geometry of the hydrodynamic and thermal model with a typical experimental image of a melt glass jet [5, 38]. (b) Numerical prediction for the evolution of the fibre diameter, when the nozzle is submitted to a convective perturbation (physical parameters may be found in Table 2) [9]

pressure, only the capillary force is to be taken into account [37].

To build dimensionless variables, we first introduce a few basic scaling parameters: length R_0 (initial radius), drawing temperature T_0 , dynamic viscosity μ_0 , density ρ and time w_0/R_0 [5, 38].

The characteristic dimensionless numbers of the problem are Reynolds, $Re = \rho w_0 R_0 / (3\mu_0)$; Nusselt, $Nu = 4.3(e^{-1} - 3e^{-3})$ with $e = \max\{3, \log(4\nu_a z / w_0 r_0^2)\}$; Prandtl, $Pr = (3\mu_0 c_P) / \lambda$ and Stanton, $St = Nu / (Re Pr)$ numbers. In the previous expressions, c_P , λ represent respectively, the heat capacity and conductivity of glass.

The dimensionless variables are the velocity, $W = w/w_0$, the radiative flux along z , that is noted Q^r . A law type Volger-Tamman-Fulcher dimensionless is chosen for the dependence of the viscosity with temperature: $M = a + b(1 - \theta)(1 - \theta_{fig})^{-1}(\theta - \theta_{fig})^{-1}$ where the glass transition temperature is taken as $\theta_{fig} = 766.88/T_0$, and for the constants: $a = -1.89$, $b = 3538.73/T_0$.

For the dimensionless external conditions, we have the ambient temperature θ_{amb} and the temperature of the thermal radiation environment θ^* .

Now for the dimensionless coefficients of the balance equations, see eq. (49), we introduce for heat transfer (free convection), $H = (\lambda_{air} Nu) / (\rho c_P w_0 R_0)$; radiative heat transfer, $E = (2\sigma T_0^3 \varepsilon(x)) / (\rho c_P w_0)$; surface tension, $\Omega = \sigma / (3\mu_0 w_0)$; forced convection, $C_1 = Re$; air shear stress, $C_2 = 2R_0 \tau_a / (3\mu_0 w_0)$;

gravity, $C_3 = \rho g R_0^2 / (3\mu_0 w_0)$; viscous diffusion $D_1 = 3\mu_0 w_0 / (\rho c_p T_0 R_0)$; thermal conduction, $D_2 = \lambda / (\rho c_p w_0 R_0)$ and the radiative transfer along z , $D_3 = \sigma_T T_0^3 / (\rho c_p w_0)$. In the previous relations, σ_T , τ_a stand for the thermal emissivity and drag coefficient. So, that we finally obtain the dimensionless mass, momentum and energy balance equations [5, 38]:

$$\begin{aligned}
 & \frac{\partial A}{\partial t} + \frac{\partial(AW)}{\partial x} = 0, \\
 & C_1 \left(A \frac{\partial W}{\partial t} + AW \frac{\partial W}{\partial x} \right) + C_2 \sqrt{A} - C_3 A = \frac{\partial}{\partial x} \left(MA \frac{\partial W}{\partial x} + \Omega \sqrt{A} \right), \\
 & A \frac{\partial \theta}{\partial t} + AW \frac{\partial \theta}{\partial x} = H(\theta_a - \theta) + E(\theta^{*4} - \theta^4) + D_1 MA \left(\frac{\partial W}{\partial x} \right)^2 \\
 & \quad + D_2 \frac{\partial}{\partial x} \left(A \frac{\partial \theta}{\partial x} \right) - D_3 A \frac{\partial A Q^r}{\partial x},
 \end{aligned}
 \tag{49}$$

where A and x represent the local dimensionless cross section and the axial coordinate, respectively. In practice, the previous equations are solved numerically using the finite-difference methods, with a Newton-Raphson, as well as substitution schemes, and with an isothermal solution as a starting condition.

This model allows predicting stationary conditions (i.e. tension, temperature, . . . that are used by the optical models, see next sub-section), as well as transient ones [9, 38]. Fig.6b shows for instance the response of the drawing system to a convective perturbation.

3.2. Modelling the light scattering properties of right circular and elliptical cylinders

For accurate optical characterizations, it is fundamental to have rigorous light scattering models. Over the years, the present authors have developed several electromagnetic models to predict the scattering properties of right circular cylinder illuminated under normal incidence [7, 39, 41]. These electromagnetic models are based on the rigorous Lorenz-Mie and Debye theories. They allow accounting for particular effects like the fibre's birefringence induced by the drawing tension as well the fibre's mean refractive index (i.e. density) with the drawing temperature and cooling rate, radial gradients, fibres with a gas core, etc. In this section, we briefly review some of these features.

During the drawing process, glass fibres are subjected to strong uniaxial mechanical constraints. Their electrical permittivity is expected to be uniaxial, too. The glass fibre material is becoming birefringent and exhibits two optical indices: one along the fibre axe (fast axis) and a second one within the fibre

cross section (two slow axes). For drawing tension of practical use, the induced birefringence depends linearly with the drawing tension. It depends also on the diameter and temperature of the fibre, as well as on its optical stress coefficient [8, 38]. For a linear polarized plane wave illuminating a fibre under normal incidence, the two permittivities corresponds to Transversal Electric (TE) and Magnetic (TM) fields, and the problem can be decoupled. Based on this scheme, we have developed code to predict both far field scattering patterns as well as the response of a phase Doppler interferometer equipped with linear analysers [7].

Due to the high cooling rate experienced by glass fibres which reach up to -10^5 °C/s in the upper region, the fibre may exhibits some radial density profiles. Our electromagnetic models take into account these effects by using a finely stratified model and a recursive algorithm [40] to cancel out the calculation of the internal electromagnetic fields. This approach allows the discretization of the fibre thermal or density gradients profiles into thousands of small increments (whose equivalent length scale is negligible, i.e. typically $\leq \lambda/40$) [41]. Although, simulations have shown that thermal gradients have a little influence on the main scattering properties of glass fibres, these simulations did show that they can significantly perturbate the morphology-dependent resonances (i.e. whispering gallery modes). This model was also used to investigate the scattering properties of hollow fibres [7, 38, 41].

The local shape of reinforcement fibre (and *a fortiori* of capillary jets) may significantly deviate from the idealized right circular cylinder one (if the process is perturbed for instance). Unfortunately, in the visible range, there is currently no solution to calculate rigorously the scattering properties of complex shaped objects whose size exceeds few microns. It is the reason why, the present authors have developed a physical optics approximation allowing describing the near-critical angle far field pattern of elliptical cylinders and ellipsoidal bubbles [14]. This model is valid for gas jets and lower density liquid jets.

3.3. Experimental methods

Experiments were carried out on a laboratory-scale single-fibre drawing bench developed by Saint-Gobain Vetrotex. The molten glass is composed of E-glass. The molten glass flows out of a resistant-heated platinum-rhodium reservoir with an initial mean velocity V_0 , through a cylindrical nozzle with an inner radius R_0 . The draw temperature T_0 of the glass leaving the nozzle is measured by a pyrometer with a resolution $T_0 = \pm 10$ °C. Two meters below the nozzle ($L = 2m$), the solidified jet is wound around a rotating drum, controlling the instantaneous take-up velocity V_f during the experiment. The

rotating drum allows the adjusting of the take-up velocity within the range $V_f = 0 - 65$ m/s with a resolution of ± 0.05 ms⁻¹ and for a drawing temperature within the range of $T_0 = 1140 - 1245$ °C, which leads to maximum drawing ratios in the range of $E \approx 3950 - 57750$ [38].

The instantaneous diameter $D_f(t)$ of the glass fibre was measured continuously in time by two laser systems specially designed for the present study, a high resolution diffractometer [9, 41] and a backward interferometer [7, 8]. The two systems use the aforementioned rigorous electromagnetic models (including all particular effects) to retrieve the fibre diameter from a diffraction pattern or Doppler signals. Note, that the backward interferometer allows also measuring simultaneously the drawing tension of the fibre with the vibration string method, as well as the axial displacement of the fibre within the optical probe volume [6, 42]. The reader is kindly invited to read the following references to get more details on the drawing bench and drawing process [5, 8, 9, 38], on the optical setups [7, 38, 41] and on scattering models [13, 14, 41].

3.4. Exemplifying experimental results

Fig. 7 shows, the evolution of the frequency and amplitude of the fibre diameter dominant oscillation mode with respect to both the Stanton number St and the draw temperature. For the Stanton number, we use the definition introduced in Shah and Pearson [34]:

$$(50) \quad St = 0.42 \frac{\lambda_{air} L}{\rho C_P} \left(\frac{2\rho_{air}}{\mu_{air}} \right)^{1/3} R_0^{-5/3} V_0^{-2/3},$$

where

ρ_{air} , $\lambda_{air} = 2.92 \cdot 10^{-4} (T_0 + 273)^{0.8}$ and $\mu_{air} = 1.58 \cdot 10^{-5} [(T_0 + 273)/300]^{1.72} \rho_{air}$ are the density, thermal conductivity and dynamic viscosity of air, while ρ and C_P are the initial molten glass density and heat capacity, respectively. In Fig. 7a, the dominant frequency decreases $\nu \approx 0.94 - 0.58$ Hz as the Stanton number increases. Conversely, the dominant frequency increases with the increasing of the draw temperature $T_0 \approx 1145 - 1245$ °C. The dominant frequency appears to be almost independent of the draw ratio. Fig. 7b shows the evolution of the mean amplitude of the fibre diameter fluctuations with respect to the draw ratio and for various Stanton numbers. Clearly, the amplitude of the diameter fluctuations decreases exponentially as the draw ratio is increased, whereas the amplitude is almost independent on the Stanton number.

The iso-level map, shown in Fig. 7c, indicates that at constant draw temperature the fibre diameter decreases rapidly as take-up velocity is increased. For a fixed take-up velocity, the diameter increases slightly with a

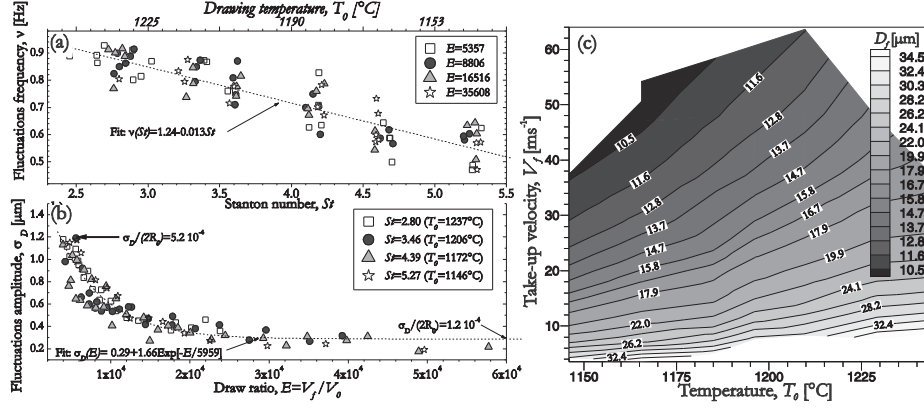


Fig. 7. Evolution of some characteristics features of the fibre diameter time series versus the drawing ratio, the drawing temperature and related Stanton numbers: (a) dominant frequency and (b) peak intensity of the diameter fluctuations; (c) Evolution of the mean diameter of the fibre versus the take-up velocity and drawing temperature [9]

Table 2. Molten glass properties and drawing parameters

Properties/Parameters	Values
Glass melt chemical composition [35]	E-glass: SiO_2 , CaO , Al_2O_3 ...
Glass melt height, H [mm]	139
Nozzle inner radius, R_0 [mm]	1.15
Viscosity, μ_0 [poises], T_0 [K]	$\log \mu_0 - 1.576 + 3027.8/(T_0 - 805.6)$
Thermal conductivity, λ [$\text{Wm}^{-1}\text{K}^{-1}$]	1.8
Heat capacity, C_P [$\text{Wkg}^{-1}\text{K}^{-1}$]	1238
Density, ρ kg^{-3}	2450
Ambient temperature, T_{amb} [K]	298

rise in temperature, reflecting the decay of the glass melt viscosity. Note, that the glass melt viscosity increases more than 100 times over the considered temperature range.

It is interesting to compare experimental results with the numerical results available in the literature concerning the stability of the glass fibre drawing process. In this field, the work of Shah and Pearson (1972) [34] is one of the most frequently referenced. A marginal stability diagram is constructed versus two parameters: $S = \bar{k}St \exp(-St)$ and the square root of the draw

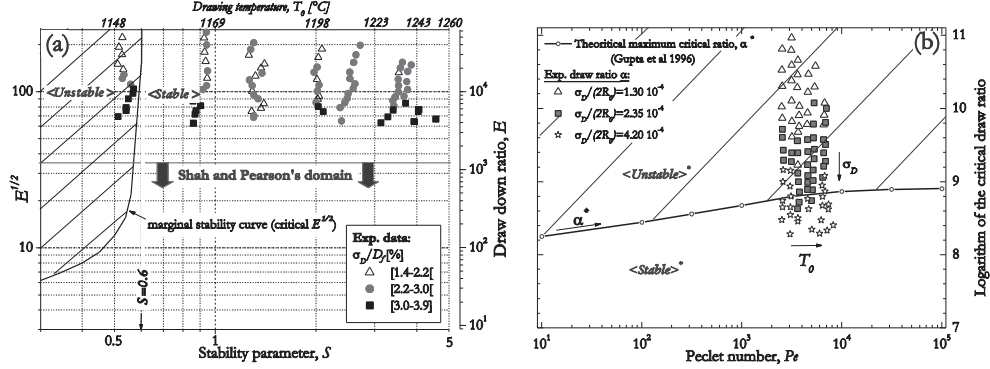


Fig. 8 (a) Location of selected experimental data points in the theoretical stability diagram [9] of Shah and Pearson [34]; (b) Same experimental data localized in the theoretical stability diagram of Gupta et al (Fig. 8 in [33])

ratio $E^{1/2}$. The dimensionless viscosity-temperature coefficient \bar{k} is defined by the equation $\bar{k} = 0.01768(T_0 - T_{amb})$ assuming a simple exponential viscosity-temperature law for the molten glass. Our experimental data points and the marginal stability curve calculated by Shah and Pearson [34] are both shown in Fig. 8a [9, 38]. The experimental data are grouped in three levels in relation to the dimensionless mean amplitude of the fibre diameter fluctuations. In the latter figure, most of our experimental data points appear in the unconditionally stable region (i.e. $S > 0.6$) except for a few points obtained for the lowest temperatures ($S < 0.6$) [34]. It is important to note, that the mean amplitude of the fibre diameter fluctuations for $S < 0.6$ is almost independent on the stability parameter S . Although, not shown in the figure, this tendency remains unchanged for the relative mean amplitude of the fluctuations. In both zones, our data points follow the general tendency of decreasing amplitude of the fluctuations as the draw ratio increases. It is worth noting that the tendency observed in the zone of expected draw resonance ($S < 0.6$) contradicts the fact that the draw resonance amplitude is known to increase as the draw ratio is increased.

In Fig. 8b the same experimental data points are plotted against Pe and $\alpha = \ln E$, where the Peclet number is defined as $Pe = \rho C_P V_0 L / \lambda$ with λ being the thermal conductivity of the molten glass. The maximum critical draw ratio curve ($\alpha^* = \ln E_{crit}^*$) extracted from Gupta et al. (Fig. 8 in [33]) is also plotted in Fig. 8b. Note, that in the calculations of Gupta et al. [33] there is no unconditionally stable zone. Experimental data points for $Pe = 4500$ deviate by up to two orders of magnitude above the theoretical maximum critical draw ratio (i.e. from $\alpha^* \approx 8.8$ to $\alpha \approx 10.8$). Although, these experimental points are

located in the zone where theoretically significant draw resonance is expected, they correspond to the lowest mean amplitude of the fibre diameter fluctuations. Furthermore, the tendency remains the same as in the unconditionally stable zone of Shah and Pearson [34] as the draw ratio is decreased. As already mentioned above, this tendency is in contradiction with the behaviour, that is known for the draw resonance zone. On the other hand, the increase of the stability range in relation to the draw ratio is not surprising as it is commonly observed in the glass fibre industry where draw ratios of $E \approx 10^5$ ($\alpha \approx 11.5$) are attained. A similar remark has been underlined by Gupta et al. [33]. To conclude, we should reject the assumption that the fibre diameter fluctuations we observed with our drawing bench (which operates in conditions close to those in industry) are the consequence of a draw resonance.

The high sizing and temporal resolution of the interferometer and diffractometer allow also controlling the drawing tension, as well the response of the drawing system to sudden perturbations. Figure 9a shows a typical evolution for the drawing tension versus the fibre diameter (i.e. the take-up velocity is continuously increased). Figure 9b shows the response of the system to a convective perturbation. The latter results show some similarities with the prediction of the hydrodynamic and thermal model, whatever the operating parameters are not exactly the same.

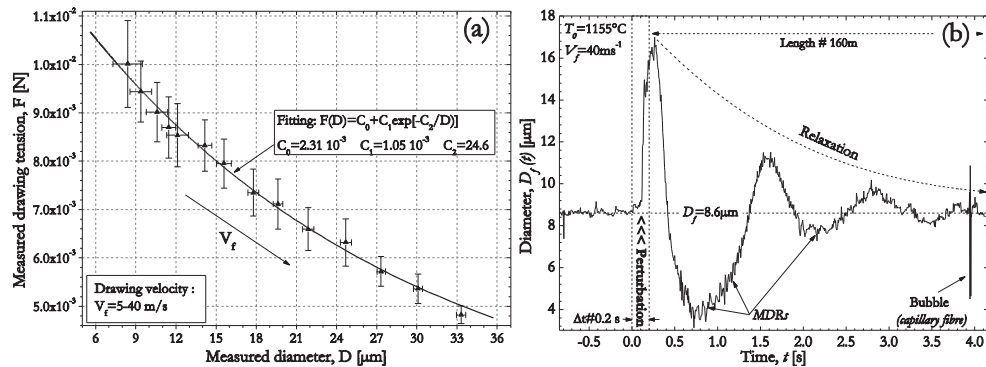


Fig. 9 (a) Typical evolution for the drawing tension with the take-up velocity (i.e. diameter) [9]; (b) Response of the system to a convective perturbation: temporal evolution of the fibre diameter when one blow on the melt glass zone [8]

4. Conclusion

In the review we summarized some of the results obtained along the collaboration IUSTI-CNRS/AMU and IMech-BAS during the period 1992–2012.

In more details, these results are given in the original papers grouped at the beginning of the list of references. The reader may find additional results, on the instability of a compound jet, in Radev et al. [4] as well as in the papers referenced there.

REFERENCES

- [1] CHACHA, M., R. OCCELLI, L. TADRIST, ST. RADEV. Disintegration of Cylindrical Liquid Columns in Liquid-Fluid Systems: Direct Numerical Simulation (and Application to Liquid Bridges). *Lect. Notes Phys.*, **467** (1996), 207–226.
- [2] CHACHA, M., ST. RADEV, L. TADRIST, R. OCCELLI. Numerical Treatment of the Instability and the Break-up of a Liquid Capillary Column in a Bounded Immiscible Phase. *Int. J. Multiphase Flow*, **23** (1997), 377–395.
- [3] RADEV, ST., M. KOLEVA, M. KASCHIEV, L. TADRIST. Initial Perturbation Effects on the Instability of a Viscous Capillary Jet, in “Recent Advances in Numerical Methods and Applications II”, (ed. Iliev et al.), World Sci., Singapore, 1999, 833–841.
- [4] RADEV, S., M. KASCHIEV, M. KOLEVA, L. TADRIST, F. ONOFRI. Numerical Analysis of the Nonlinear Instability of One-Dimensional Compound Capillary Jet. *Lect. Notes Comput. Sci.*, **1988** (2001), 692–701.
- [5] LENOBLE, A., F. ONOFRI, S. RADEV. Modélisation physique du procédé des fibrage des fibres de renforcement, Proceeding of the Congrès Français de Thermique, Vittel-France, 3–6 juin, 2002, 139–144.
- [6] ONOFRI, F., A. LENOBLE, S. RADEV. Superimposed Non Interfering Probes to Extend the Phase Doppler Anemometry Capabilities. *Appl. Opt.*, **41** (2002), No. 18, 3590–1600.
- [7] ONOFRI, F., A. LENOBLE, S. RADEV, H. BULTYNCK, P.-H. GUERING, N. MARSAULT. Interferometric Sizing of Single-axis Birefringent Glass Fibres, *Part. Part. Syst. Char.*, **20** (2003), No. 3, 171–182.
- [8] ONOFRI, F., A. LENOBLE, S. RADEV, P.-H. GUERING. Optical Measurement of the Drawing Tension of Small Glass Fibres. *Meas. Sci. Technol.*, **15** (2004), 1279–1284.
- [9] ONOFRI, F., A. LENOBLE, S. RADEV, P.-H. GUERING. High Resolution Monitoring of an Unsteady Glass Fibre Drawing Process. *Exp. Fluids*, **42** (2007), 601–610.
- [10] RADEV, S., L. TADRIST, F. ONOFRI. Sinuous Instability of a Viscous Capillary Jet injected into an Immiscible Non-viscous Fluid. PART I: 3D-equation of Motion of a Slender Jet in the Moving Trihedron of the Jet Axis. *J. Theoret. Appl. Mech.*, **37** (2007), No. 1, 23–38.

- [11] RADEV, S., F. ONOFRI, L. TADRIST. Sinuous Instability of a Viscous Capillary Jet injected into an Immiscible Non-viscous Fluid. PART II: Different Forms and Numerical Analysis of the Numerical Analysis of the Dispersion Equation. *J. Theoret. Appl. Mech.*, **37** (2007), No. 2, 3–15.
- [12] RADEV, S., K. NACHEV, F. ONOFRI, L. TADRIST, A. LIOLIOS. Numerical Analysis of the Sinuous Instability of a Viscous Capillary Jet Flowing Down an Immiscible Nonviscous Fluid. *Lect. Notes Comput. Sci.*, **4310** (2007), 677–684.
- [13] ONOFRI, F. R. A., M. KRZYSIEK, J. MROCZKA, K.-F. REN, ST. RADEV, J.-P. BONNET. Optical Characterization of Bubbly Flows with a Near-critical-angle Scattering Technique. *Exp. Fluids*, **47** (2009), No. 4, 721–732.
- [14] ONOFRI, F. R. A., ST. RADEV, M. SENTIS, S. BARBOSA. A Physical-optics Approximation of the Near-critical-angle Scattering by Spheroidal Bubbles. *Opt. Lett.*, **37** (2012), No. 22, 4780–4782.
- [15] RAYLEIGH, L. On the Instability of Jet. *Proc. Lond. Math. Soc.*, **10** (1878), 4–13.
- [16] MCCARTHY, M. J., N. A. MOLLOY. Review of Stability of Liquid Jets and the Influence of Nozzle Design. *Chem. Eng.*, **7** (1974), 1–20.
- [17] SHOKOOHI, F. Numerical Investigation of the Disintegration of Liquid Jets, Ph.D. thesis, New York, Colombia University.
- [18] SHOKOOHI, F., H. G. ELROD. Numerical Investigation of the Disintegration of Liquid Jets. *J. Comp. Phys.*, **71** (1987), 324–342.
- [19] TOMOTIKA, S. On the Instability of a Cylindrical Thread of a Viscous Liquid surrounded by Another Viscous Fluid. *Proc. R. Soc. Lond. A*, **10** (1935), 322–337.
- [20] MIKAMI, T., S. G. MASON. Capillary Breakup of a Binary Liquid Inside a Tube. *Can. J. Chem. Eng.*, **53** (1975), 372–377.
- [21] KITAMURA, Y., H. MICHIMA, T. TAKAHASHI. Stability of Jets in Liquid-liquid Systems. *Can. J. Chem. Eng.*, **60** (1982), 723–731.
- [22] DEBYE, P., J. DAEN. Stability Considerations on Nonviscous Jets exhibiting Surface or Body Tension. *Phys. Fluids*, **2** (1959) 416–421
- [23] MARTINON, J. Stability of Capillary Cylindrical Jets in External Flow. *J. Appl. Math. Phys.*, **34** (1983), 575–582.
- [24] GODELLE, J. Analyse non Linéaire de Dynamiques de Jets Liquides Cylindriques, PhD thesis (in French), France, Université de Rouen, 1999.
- [25] TADRIST, L., E. K. O. ALAOUI, R. OCCELLI, J. PANTALONI. Experimental Study of a Liquid Jet flowing into Another Immiscible Liquid: A Local Analysis of the Interface. *Exp. Fluids*, **12** (1991), 67–75.
- [26] YARIN, A. L., P. GOSPODINOV, O. GOTTIEB, M. D. GRAHAM. Newtonian Glass Fiber Drawing : Chaotic Variation of the Cross Section Radius. *Phys. Fluids*, **11** (1999), 3201–3208.
- [27] TYUSHKEVICH, N. I., A. S. KRAS'KO, A. A. CHEPURKIN, O. P. SHIMAN, T. O. KOZELLO, N. A. ANANICH. Study of the Unevenness of Glass Fiber by Statistical Methods. *Glass and Ceramics*, **27** (1970), 95–97.
- [28] GLIKSMAN, L. R. The Dynamics of a Heated Free Jet of Variable Viscosity Liquid at Low Reynolds Numbers. *J. of Basic Eng.*, **15** (1968), 343–354.

- [29] DONNELLY, G. J., C. B. WEINBERGER. Stability of Isothermal Fiber Spinning of a Newtonian Fluid. *Ind. Eng. Chem. Fundam.*, **14** (1975), 334–337.
- [30] FISHER, R. J., M. M. DENN. A Theory of Isothermal Melt Spinning and Draw Resonance. *AIChE J.*, **22** (1976), 236–246.
- [31] GEYLING, F., T., G. M. HOMS. Extensional Instabilities of the Glass Drawing Process. *Glass Technol.*, **21** (1980), 95–102.
- [32] SCHULTZ, W. W., S. H. DAVIS. Effects of Boundary Conditions on the Stability of Slender Viscous Fibers. *J. Appl. Mech.*, **106** (1984), 1–5.
- [33] GUPTA, G. K., W. W. SCHULTZ, E. M. ARRUDA, X. LU. Nonisothermal Model of Glass Fiber Drawing Stability. *Rheol. Acta*, **35** (1996), 584–596.
- [34] SHAH, Y. T., J. R. A. PEARSON. On the Stability of Non-isothermal Fibre Spinning. *Ind. Eng. Chem. Fundam.*, **11** (1972), 145–149.
- [35] GUPTA, P. K. Fibres Reinforcements for Composite Materials, In: Fibres Reinforcements for Composite Materials, Chap. 2, (Ed. Bunsell A. R.). Amsterdam, Elsevier, 1988.
- [36] TOUTIRI, C. Modélisation Dynamique et Thermique d’une Fibre de Verre en Cours D’étirage, PhD. Thesis (in French), France, Poitiers, University of Poitiers, 1999.
- [37] MIDDLEMAN, S. Modeling Axisymmetric Flows: Dynamics of Films, Jets, and Drops, Academic Press, 1995.
- [38] LENOBLE, A. Caractérisation optique d’une fibre de verre en cours de fibrage: contribution à l’étude de la stabilité du procédé, PhD thesis (in French), University of Provence, France, 2004.
- [39] ONOFRI, F., L. BERGOUNOUX, J.-L. FIRPO, J. MESGUISH-RIPAULT. Velocity, Size and Concentration Measurements of Optically Inhomogeneous Cylindrical and Spherical Particles. *Appl. Opt.*, **38** (1999), No. 21, 4681–4690.
- [40] ONOFRI, F., G. GRÉHAN, G. GOUESBET. Electromagnetic Scattering from a Multilayered Sphere Located in an Arbitrary Beam. *Appl. Opt.*, **34** (1995), No. 30, 7113–7124.
- [41] ONOFRI, F., A. LENOBLE, B. BULTYNCK, P.-H. GUÉRING. High-resolution Laser Diffractometry for the On-line Sizing of Small Transparent Fibres. *Opt. Commun.*, **234** (2004), 183–191.
- [42] ONOFRI, F. Three Interfering Beams in Laser Doppler Velocimetry for Particle Position and Microflow Velocity Profile Measurements. *Appl. Opt.*, **45** (2006), No. 14, 3590–1600.